JOURNAL OF
Materials
CHEMISTRY

Microstructural development of the $La_{0.5}Li_{0.5}TiO_3$ lithium ion conductor processed by the laser floating zone (LFZ) method†

Alejandro Várez,*[a] María L. Sanjuán,[b] María A. Laguna,[b] Jose I. Peña,[c] Jesús Sanz[d] and German F. de la Fuente[c]

[a] *Departamento de Materiales, Universidad Carlos III de Madrid, Avda. Universidad, 30, 28911 Leganés, Spain. E-mail: alvar@ing.uc3m.es*
[b] *Instituto de Ciencia de Materiales de Aragón, CSIC-Universidad de Zaragoza, 50009 Zaragoza, Spain*
[c] *Instituto de Ciencia de Materiales de Aragón, CSIC-Universidad de Zaragoza, 50015 Zaragoza, Spain*
[d] *Instituto de Ciencia de Materiales de Madrid, CSIC, 28049 Cantoblanco, Spain*

Received 25th April 2000, Accepted 6th July 2000
First published as an Advance Article on the web 12th October 2000

$La_{2/3-x}Li_{3x}TiO_3$ ($0<x<0.17$) compounds have reached great prominence in the last few years due to their high lithium ion conductivity. They present a perovskite-related structure (ABO_3) with A-cation deficiency. However, neither the phase diagram nor the solidification processes are well known, which makes the growth of single crystals difficult. In this vein, we have processed $La_{0.5}Li_{0.5}TiO_3$ polycrystalline powder by the LFZ method and studied the processed material by means of SEM, EDS, XRD and micro-Raman techniques. Three phases have been detected: the major phase (A) is a La–Li–Ti–O perovskite with $3x<0.5$, that forms large single crystal grains. Phase B is rutile TiO_2 and appears as small precipitates surrounding phase A. Finally, we observe eutectic mixtures of phase A and a third phase (C) containing Ti and O in a ratio lower than 1 : 2. Phase C is identified as a Li–Ti oxide, probably $Li_2Ti_3O_7$.

Introduction

Li ion-conducting materials have been widely studied in the last few years because of their potential applications as solid electrolytes in high energy batteries and other electrochemical devices. Nowadays one of the best Li ion conductors at room temperature is found in oxides with a perovskite related structure[1–5] with the general formula $La_{2/3-x}Li_{3x}TiO_3$. Although these materials present a relatively wide range of Li solutions the limits are under discussion. Robertson *et al.*[3] have published a tentative phase diagram where the minimum and the maximum solubilities of Li were established as $x=0.04$ and 0.14 respectively. Fourquet *et al.*[4] found a slightly narrower composition range ($0.06 \leqslant x \leqslant 0.14$), while Kawai and Kuwano[2] expand the upper limit up to $x=0.15$. These small differences could be attributed to the slightly different synthesis conditions employed. In all the cases mentioned, the structural model proposed for samples at room temperature was a perovskite doubled along the *c*-axis with tetragonal symmetry.

Recently, we found that the compositional range could be enlarged in both limits ($0.03 \leqslant x \leqslant 0.167$) by heating up to 1350 °C.[6,7] We have also observed, by means of X-ray diffraction experiments, a change of symmetry from tetragonal to orthorhombic of the doubled unit cell when the Li content decreases below $x=0.06$. These structural modifications are associated with cation vacancies ordering along the *c*-axis into two alternating A sites of the perovskite (ABO_3). This ordering disappears gradually with the lithium content and with the temperature. When the Li-rich end member ($x=0.167$) is quenched from 1300 °C into liquid nitrogen, a primitive cubic cell, ($a_p \times a_p \times a_p$), with a unique A site is detected by X-ray diffraction experiments.[6] However, the neutron diffraction (ND) pattern of this sample was indexed in a hexagonal unit cell (space group *R*-3*c*). Rietveld refinement of ND data indicated that La ions occupy the A site, while Li cations are fourfold oxygen coordinated at the centre of square faces of the cubic perovskite.[8] As a consequence of this fact the number of vacancies of perovskite is higher than that deduced in former structural analyses where La and Li occupied A sites.

The aim of the present work has been to grow monocrystalline fibers of the fast ionic conductor $La_{2/3-x}Li_{3x}TiO_3$ ($x=0.167$) to study the phase diagram under directional solidification.

Experimental

1 Crystal growth

1.1 Precursor rod preparation. The precursors were obtained from $La_{0.5}Li_{0.5}TiO_3$ powders prepared by conventional solid-state reaction on Al_2O_3 crucibles, following the literature procedures.[1,6,9] These powders were finely ground in acetone using an agate ball mill, and then isostatically pressed at room temperature inside a latex tube with an applied pressure of 250 MPa. Cylinder shaped samples with a typical diameter of 3 mm and up to 50 mm in length were obtained. These ceramic precursors were heated in air up to 1350 °C for 6 hours. In order to avoid lithium losses the heating rate used during the synthesis of the $La_{0.5}Li_{0.5}TiO_3$ powders and during the sintering of the precursor was 1 °C min^{-1}.

1.2 Crystal growth by the laser floating zone technique. Fibers of $La_{0.5}Li_{0.5}TiO_3$ were grown by the laser floating zone technique (LFZ) as described elsewhere.[10] It is a crucible-free technique of crystal growth where a well-defined, small volume of material is molten and moved upwards along a compact

---

†Basis of a presentation given at Materials Discussion No. 3, 26–29 September, 2000, University of Cambridge, UK.

DOI: 10.1039/b003305g

This journal is © The Royal Society of Chemistry 2001

powder rod. The CO_2 laser radiation, adequately focused by standard optical elements, provides control over the crystal–melt interface during growth and allows the growth of high purity crystals in rod form and with uniform diameter. Once the precursor is mounted onto the upper and lower part of the vertical axis inside the growth chamber, this is evacuated and refilled with a N_2/O_2 synthetic air mixture. Travelling rates of 50 mm h^{-1} were used to grow the fibers. Lower rates increase the volatilisation of the mixtures due to the longer times that the material is in the melt state. Once the growth comes to an end the movement of the sample is stopped at the same time as the laser radiation is switched off obtaining a frozen zone on top of the fiber.

For subsequent characterisation and convenience in handling, the fibers were mounted in a matrix of thermosetting polymer that was cured under pressure and temperature simultaneously. Afterwards the mounted fiber was cut in a transverse and a longitudinal direction. Finally it was subjected to grinding and polishing with diamond paste.

2 Characterisation

X-Ray diffraction (XRD) patterns were recorded with CuKα radiation in an X'Pert Philips diffractometer, with ($\theta/2\theta$) Bragg–Brentano geometry, equipped with a curved graphite monochromator. The mounted fiber was located into a multipurpose stage that enables the XRD analysis of large three-dimensional samples. Data were taken with a 0.5° divergence slit, a receiving slit of 0.01° and a set of soller slits with an axial divergence of 1°. The 2θ range analysed was 10–90°, with a step scan of 0.02 and a counting time of 5 s for each step. The working conditions were 40 kV and 55 mA.

A Philips XL30 scanning electron microscope equipped with a backscattered (BSE) and an energy dispersive X-ray (EDAX) detector was employed to study the microstructure and composition of the fibers. The microscope almost always operated in the backscattered mode between 15–20 kV, and all the EDAX analyses were registered at the same conditions of voltage (20 kV), take-off angle and live time. For each different phase observed on the BSE images, four independent analyses were carried out. Stoichiometric samples of Li_2TiO_3, $Li_2Ti_3O_7$ and $La_2Ti_2O_7$ were used as the standards for Li, Ti and La determination.

Raman spectroscopy experiments were performed at room temperature in a Dilor XY spectrometer with a diode array multichannel detector. Light from a coherent Ar^+ laser at 514.5 nm was focused onto the sample through a × 50 or a × 100 microscope objective lens, providing a maximum spatial resolution of about 2 μm. A confocal diaphragm was sometimes used to gain in-depth resolution. The light power at the sample was 10 mW and the spectral resolution was typically 3 cm^{-1}.

Results

a X-Ray diffraction experiments

Fig. 1 shows the X-ray diffraction (XRD) patterns of the longitudinal and cross-section of the fiber as well as the starting polycrystalline material. In the case of the longitudinal section of the fiber, most of the diffraction peaks are coincident in position with those of the polycrystalline material, while the intensities are quite different. This is due to the preferential orientation of the samples during the directional solidification. This fact is more appreciable in the XRD pattern of the cross-section of the fiber, where the peaks corresponding to the (112) and (224) planes of the tetragonal perovskite are the most important. Likewise extra diffraction peaks ($2\theta \approx 26.5$ and 38.8) are observed that we attribute to the secondary phases detected on the BSE micrograph (see below).

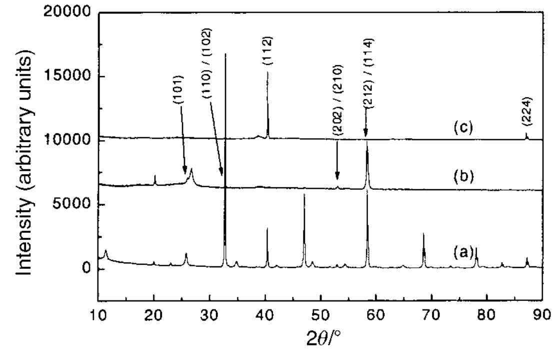

Fig. 1 Experimental X-ray diffraction patterns for: (a) starting material, and (b) longitudinal and (c) cross-sections of the mounted grown fiber. The different intensities of the peaks are attributed to the anisotropy of the grown fiber.

b Microstructural study

Fig. 2 shows a backscattered electron (BSE) micrograph of a longitudinal section of the grown fiber. Three different areas can be distinguished: a) the quenched or frozen zone (right), that corresponds to the last liquid part of the material just before switching off the laser, b) the fiber grown by directional solidification (left) and c) the solidification interface (liquid phase interface during the fiber growth).

In the case of the grown fiber area, we can see large grains (white contrast) oriented along the growth direction. Surrounding these columnar grains, dark contrast areas can be distinguished which have been assigned to secondary phases. A magnification of the interface zone (Fig. 3) shows a eutectic morphology, where white and black layers alternate. The lamellar spacing in this case is very small indicating that the solidification rate was rather high.

The frozen zone presents a branch-out morphology with a very high degree of disorder where different phases (areas with black and white contrast on the BSE image) coexist indicating a phase separation. The presence of intermixed phases provides better mechanical properties. In fact, in this area no cracks, arising from the polishing process, are detected. At higher magnification (Fig. 4) we can see how the primary crystals (white contrast) grow from the liquid in a dendritic manner. Solidification starts at a nucleus in the interface area and quickly grows parallel to the fiber. Subsequently, secondary arms grow perpendicular, in some cases, and at 45°, in others, producing dendrite-type crystals. Between these white contrast branches, the residual liquid (dark contrast) with a composition different from that of the primary dendrites, has been

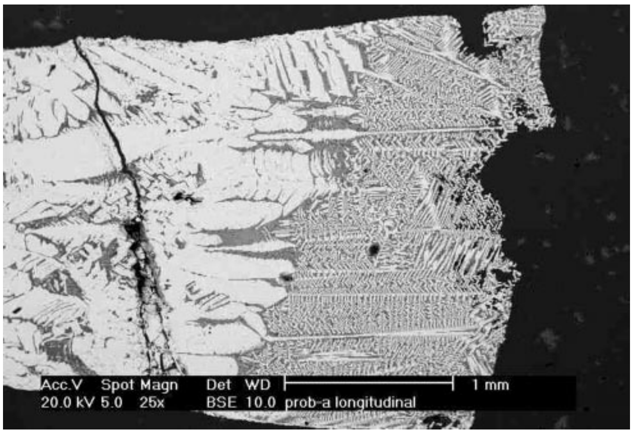

Fig. 2 Scanning electron micrograph in the backscattered (BSE) mode of a longitudinal section of the mounted fiber. Three different zones can be distiguished: frozen zone (right), grown fiber (left) and the narrow interface of solidification (middle).

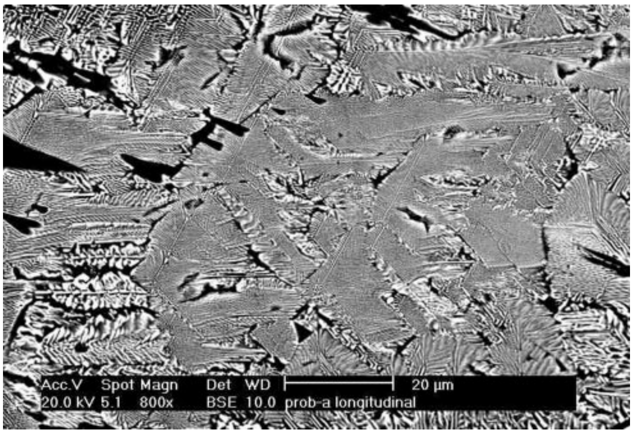

Fig. 3 Magnification of the black contrast area that appears in the interface of solidification of Fig. 2.

solidified. It is worth noting that the dark contrast area is more abundant in the frozen than in the grown fiber areas.

In Fig. 5a a cross-section of the grown fiber is presented. At low magnification "equiaxial" grains (white contrast) can be observed. These correspond to the columnar grains detected on the longitudinal section. The grain boundaries present a black contrast that, at higher magnification (Fig. 5b), shows a eutectic aspect. We can also distinguish grey contrast areas appearing like a segregated phase.

c X-Ray microanalysis

In order to know the composition of the different phases emerging during the solidification, we have performed microanalyses in the different areas by means of EDS. In Table 1, we present the elements detected and their proportions.

Taking into account the limitations of the technique, related to the detection of light elements and the absorption problem of La, we could deduce the following:

(1) The primary crystals (white contrast) correspond to the major phase of the grown fiber and also participate as a eutectic constituent. All the crystals present an excess of La in relation to the starting material.

(2) The grey contrast phase presents a stoichiometry close to that of titanium dioxide.

(3) The composition of the black contrast area is similar to that of the grey contrast phase, however the amount of oxygen is slightly higher and always 2–3 wt% of Al, coming from the crucible, is present.

d Micro-Raman spectroscopy experiments

We have measured the Raman spectra of the different phases present in the fiber. The experiments were performed in parallel to scanning electron microscopy analysis and led to the following observations.

In Fig. 6A Raman spectra corresponding to the major phase (white contrast) of the processed fiber are presented. A comparison with those spectra of the La$_{2/3-x}$Li$_{3x}$TiO$_3$ series (Fig. 6B) shows that the lithium content of the main phase is $0.1 < 3x < 0.3$. much smaller than the starting value $3x = 0.5$. On the other hand, it must be noted that, within a single grain, the spectrum changed on going from the middle to the outside, denoting a possible increase of lithium content in the perovskite when approaching the single crystal boundary (note the resemblance of spectra labelled (c) in Figs. 6A and 6B).

Each individual grain proved to be a single crystal with clear polarisation properties in the Raman spectra. Within a given grain of the cross-section, the orientational dependence of the spectrum is the one expected for rotation in the (112) plane. This is consistent with the XRD result that in this section the majority of grains present a (112) plane orientation.

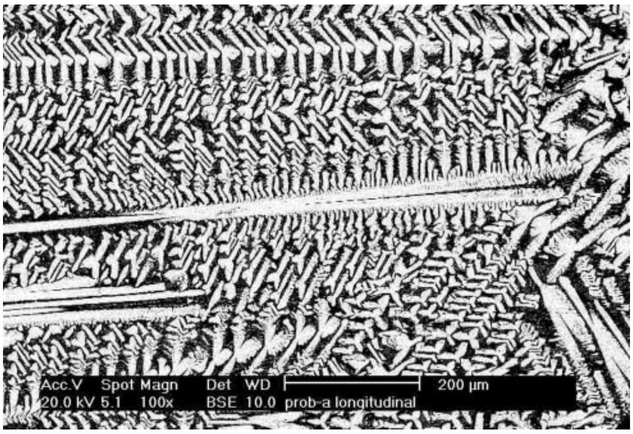

Fig. 4 Magnification of a zone of the frozen part in Fig. 2, showing the microstructure of solidifying.

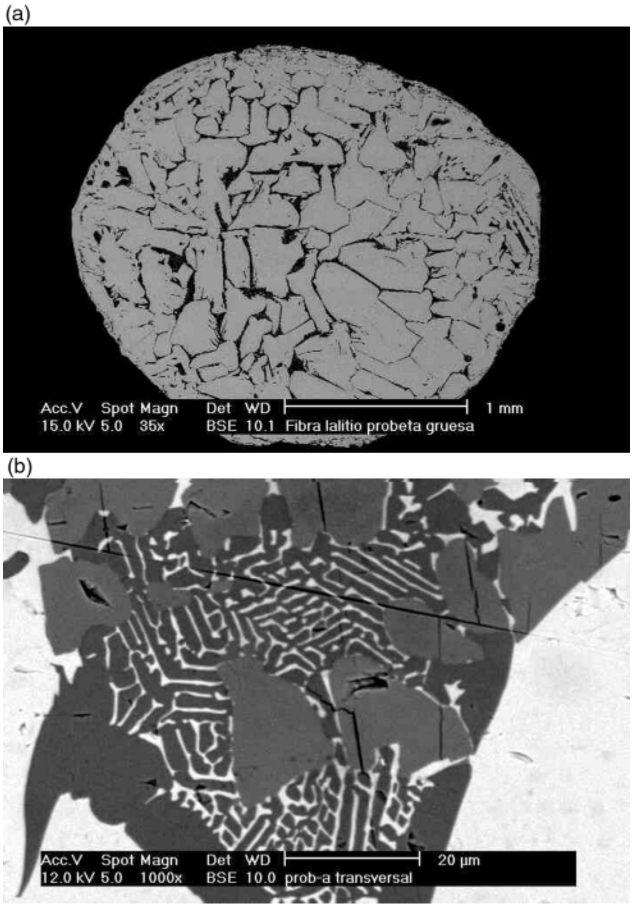

Fig. 5 Transverse section of the fiber at low (a) and high (b) magnification. Three different contrasts, corresponding to three phases, can be observed at higher magnification: grey (segregated grains of titanium dioxide), white (La–Li–Ti–O perovskite) and black (lithium titanium oxide). The last two phases solidify in a eutectic manner.

At least three different spectra were found in the dark contrast inclusions appearing between the major phase grains. The grey contrast phase, with a Ti : O proportion close to 2, was unambiguously identified as rutile TiO$_2$[11] (Fig. 7a). In the quenched zone the spectrum of TiO$_2$ anatase was also found[12] (Fig. 7b). The black contrast phase gave a weakly active broad spectrum, frequently superposed to peaks of the La–Li–Ti–O phase or of TiO$_2$. With the use of a confocal diaphragm we have been able to isolate the spectrum of the pure dark contrast phase (see Fig. 8A) and identify it as that of a Li–Ti oxide. A comparison with reference spectra shown in Fig. 8B suggests

Table 1 EDAX semiquantitative analysis of different phases observed in the grown fiber (Relative errors in La, Ti and O were lower than 5, 3 and 8%)

Area	Phase	Elements	Ratio	Remarks
Frozen	White	La : Ti : O	0.7 : 1 : 3.1	
	Grey	Ti : O	1 : 1.8	
	Black	(Ti + Al) : O	1 : 2.1	2–3 wt% Al
Interface	Lamellar	La : Ti : O	0.2 : 1 : 2.6	Mixture of white and black phases
Grown fiber	White	La : Ti : O	0.7 : 1 : 3.1	
	Grey	Ti : O	1 : 1.9	
	Black	(Ti + Al) : O	1 : 2.3	2–3 wt% Al

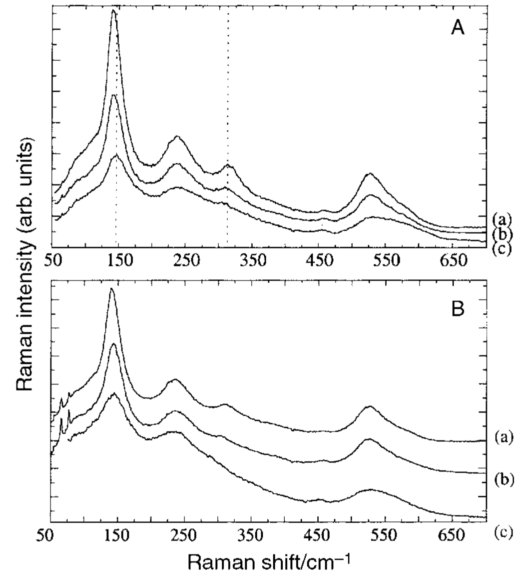

Fig. 6 (A) Raman spectra taken along a single grain of the white contrast phase, in the transverse section of the fiber. The experimental conditions were exactly the same in all three cases but from (a) to (c) spectra were taken increasingly close to the dark contrast inclusions. They are interpreted as due to $La_{2/3-x}Li_{3x}TiO_3$ perovskite with increasing lithium content. (B) Room temparature Raman spectra of $La_{2/3-x}Li_{3x}TiO_3$ ceramics with varying lithium content: (a) $3x = 0.12$; (b) $3x = 0.18$; (c) $3x = 0.5$. All three samples were prepared under similar experimental conditions.

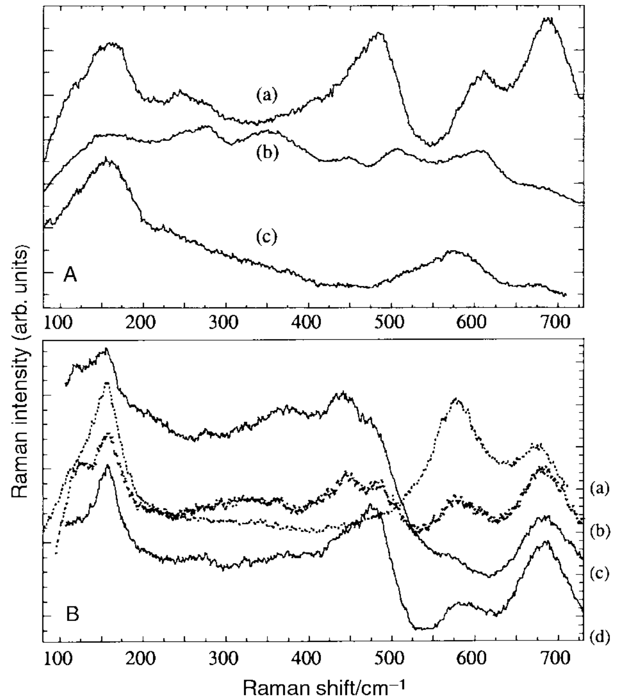

Fig. 8 (A) Spectra of the dark contrast phase taken at two different points of the transverse section. Spectra (a) and (b) correspond to parallel and crossed polarisation measurements in an isolated dark inclusion and (c) was taken in a parallel configuration in the dark contrast area at the left of the inclusion seen in Fig. 5b. (B) Raman spectra of ceramic samples of slowly cooled (a,c,d) and quenched (b) $Li_2Ti_3O_7$. Spectra (c) and (d) were taken in crossed and parallel configurations, respectively, on the same point of the sample, while (a) was taken on a different point. Quenched $Li_2Ti_3O_7$ gave spectra similar to (b) throughout the whole sample.

that it may be $Li_2Ti_3O_7$ with ramsdellite structure. However, the appearance of weak reflections in the XRD patterns close to those of the high temperature phase of Li_2TiO_3[13] adds the possibility of having this Raman inactive or weakly active phase in the fiber.

In the eutectic regions formed by white and black contrast phases the spectrum was a superposition of those of the white and black contrast phases, La–Li–Ti–O and Li–Ti–O (see Fig. 9). A comparison of this spectrum with those of ceramic powders of the same system (see Fig. 6B) allows us to conclude that the La–Li–Ti oxide in the eutectic precipitates presents a higher degree of disorder and lithium content than the same phase forming the large white contrast grains.

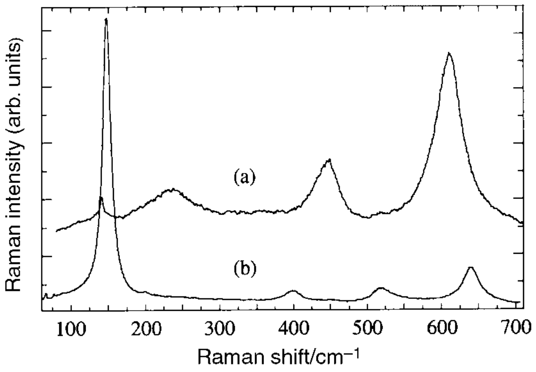

Fig. 7 Spectra of TiO_2 rutile (a) and anatase (b). Rutile was found either in the quenched or grown sections of the fiber and corresponds to the grey contrast phase of microanalysis; anatase was found only in the quenched region.

Discussion

Scanning electron microscopy experiments show that monocrystalline fibers can be grown by the LFZ technique. Fibers are formed by relatively large rod-like single crystals (0.5–1 mm in length × 0.2–0.5 mm in diameter) of the major perovskite phase aligned parallel to the growth direction. The lithium content of these crystals is lower than the one of the precursor and they have been grown from a liquid phase.

During the processing of the fiber, TiO_2 is segregated from the liquid, appearing as a proeutectic precipitate, and some Li_2O is probably lost by volatilisation. At the same time, the lithium and titanium content of the liquid increases up to the eutectic composition. This liquid then freezes surrounding the single crystals of the major phase to form a eutectic mixture. From X-ray microanalysis and Raman spectroscopy results,

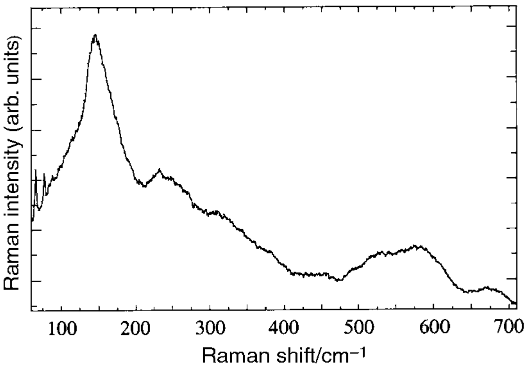

Fig. 9 Spectrum taken in the eutectic region at the centre of the inclusion seen in Fig. 5b, close to the point where spectrum (c) of Fig. 8 was measured. It can be explained as a superposition of the spectra from the white and dark contrast phases.

described above, we identified that a Li–Ti oxide, probably $Li_2Ti_3O_7$ (black contrast in BSE images) and the major phase lithium perovskite (white contrast) form the eutectic microstructure. In this sense we can propose the following solidification sequence:

$$L \rightarrow P_0 + TiO_2 + L' \quad (1)$$

$$L' \rightarrow (L\text{–}Ti\text{–}O + P_e)_{eutectic} \quad (2)$$

where L and L′ correspond to liquid phases with different compositions, P_0 corresponds to the lithium deficient perovskite (major phase) and P_e to the lithium rich perovskite forming the eutectic mixture. This small amount of TiO_2 proeutectic phase is consistent with either some loss of lithium or lithium enrichment of the remaining liquid in order to produce the eutectic reaction.

The suggested solidification process, shown in Fig. 10, is partially in consonance with the results of Robertson *et al.*[3] These authors studied the Li_2TiO_3–$La_{2/3}TiO_3$ pseudo-binary phase diagram, from samples prepared by solid-state reactions and pointed out the presence of a eutectic ($A + Li_2TiO_3$) mixture, where A corresponds to a cubic phase with a composition close to $La_{0.525}Li_{0.425}TiO_3$. In our results, Raman spectra arising from the white phase of the eutectic microstructure are quite similar to those of La–Li–Ti–O ceramic powders with high lithium content. However, the eutectic temperatures predicted by those authors (1275 ± 25 °C) are too low. In fact, we have never found any sign of a liquid phase during the sintering of the precursor at 1350 °C, and we have increased the temperature up to 1700 ± 50 °C in order to melt the rod-like precursor and grow the fiber. The reason is probably that the eutectic composition is considerably shifted toward the lithium rich end, midway between Li_2TiO_3 and $La_{0.5}Li_{0.5}TiO_3$, as can be deduced from the BSE images.

As we have mentioned before the lithium content of the liquid phase increases during the processing of the fiber, as can be deduced from the fact that the black contrast area (lanthanum free), detected in the BSE micrographs, is more abundant in the frozen area than in the grown fiber. The presence of a high amount of lithium in the liquid reduces the solidification temperature operating as a flux.

On the other hand, the presence of TiO_2 anatase in the frozen area indicates that this phase is stabilised at higher temperature and the rapid cooling retains that structure.

Another important aspect is the anisotropy of the fibers. This fact can be deduced from the big difference between the transverse and longitudinal XRD patterns of the fibers. As we have mentioned before, in the first case, the most intense peaks correspond to the (112) and (224) planes of the tetragonal cell and the (111) and (222) of the cubic perovskite. These planes correspond to the AO_3 close packed layers of the perovskite. This fact allows us to explain the morphology of the grain boundary in Fig. 5a, where angles of 120° are mostly found.

The aluminium detected in the analysis of the dark contrast phase is attributed to the crucible used in the synthesis of the precursor. The presence of this element in perovskite single-crystals is not discarded and might explain some minor frequency shifts observed when comparing the present Raman spectra with those of the $La_{2/3-x}Li_{3x+y}Ti_{1-y}Al_yO_3$ ceramics. However, the high atomic weight of lanthanum prevents the detection of aluminium in the above phase by the EDS technique. We have never detected Al in rutile TiO_2, probably due to the lack of solubility of this cation in the rutile network, while Al is easily soluble in the Li_2TiO_3 and $Li_2Ti_3O_7$ structures.[14]

Conclusions

The laser floating zone (LFZ) technique has been successfully employed to grow fibers of the $La_{0.5}Li_{0.5}TiO_3$ fast ionic conductor. The microstructure of these processed materials presents relatively large single crystals of a lithium deficient Li–La–Ti–O perovskite. In the boundary of these large crystals, signs of a liquid phase have been observed where a eutectic reaction takes place. The eutectic components have been identified as lithium rich perovskite and a Li–Ti oxide, probably $Li_2Ti_3O_7$.

The obtained fibers present a strong anisotropy since they grow parallel to the [111] direction of the single-cubic perovskite [close packed layer (LaO_3) stacking direction]. Taking into account that the growth of single crystals of these materials has not been successfully developed, this technology opens new possibilities for the characterisation of this kind of compound where the mechanism of the high lithium ion conductivity has not yet been established.

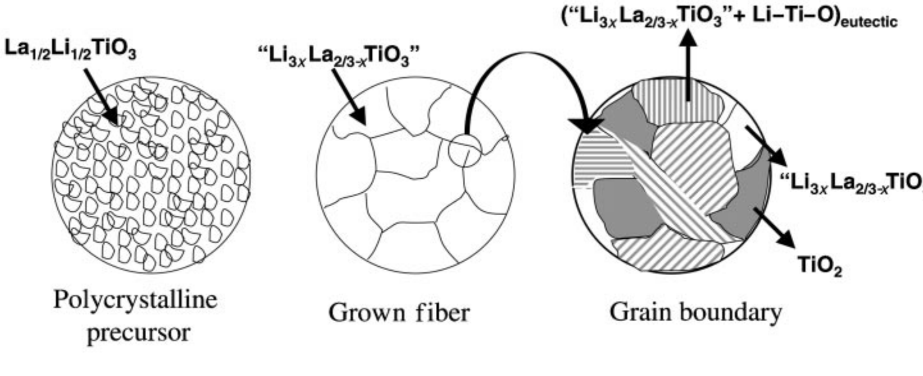

Fig. 10 Schematic representation of the developed microstructure before and after fiber growth.

References

1 Y. Inaguma, C. Liquan, M. Itoh, T. Nakamura, T. Uchida, H. Ikuta and M. Wakihara, *Solid State Commun.*, 1003, **86**, 689.

2 H. Kawai and J. Kuwano, *J. Electrochem. Soc.*, 1994, **141**, L78.

3 A. D. Robertson, S. García-Martín, A. Coats and A. R. West, *J. Mater. Chem.*, 1995, **5**, 1405.

4 J. L. Fourquet, H. Duroy and M. P. Crosnier-López, *J. Solid State Chem.*, 1996, **127**, 283.

5 C. Leon, M. L. Lucia, J. Santamaría, M. A. París, J. Sanz and A. Várez, *Phys. Rev. B*, 1996, **54**, 183.

6 J. Ibarra, A. Várez, C. León, J. Santamaría, L. M. Torres-Martínez and J. Sanz, *Solid State Ionics*, 2000, in press.

7 M. A. París, J. Sanz, C. León, J. Santamaría, J. Ibarra and A. Várez, *Chem. Mater*, 2000, **12**, 1694.

8 J. A. Alonso, J. Sanz, J. Santamaría, C. León, A. Várez and M. T. Fernández-Díaz, *Angew. Chem., Int. Ed.*, 2000, **39**, 619.

9 A. Várez, F. García-Alvarado, E. Morán and M. A. Alario-Franco, *J. Solid State Chem.*, 1995, **118**, 78.

10 G. F. de la Fuente, J. C. Diez, L. A. Angurel, J. I. Peña, A. Sotelo and R. Navarro, *Adv. Mater.*, 1995, **8**, 853.

11 G. A. Samara and P. S. Peercy, *Phys. Rev. B*, 1973, **7**, 1131.

12 T. Ohsaka, F. Izumi and Y. Fujiki, *J. Raman Spectrosc.*, 1978, **7**, 321.

13 E. Kordes, *Fortschr. Mineral.*, 1933, **18**, 27.

14 K. H. Kim and F. A. Hummel, *J. Am. Ceram. Soc.*, 1960, **43**, 611.